Materials & Design 245 (2024) 113237

Contents lists available at ScienceDirect

Materials & Design

journal homepage: www.elsevier.com/locate/matdes

# Hydrogen production from wastewater using interdigitated printed electrode-based Single-Chamber microbial electrolysis cells

Vikash Kumar [a], Malaya Prasad Behera [a], Yifan Lv [a], Banu Pradheepa Kamarajan [b], Sarat Singamneni [a,*]

[a] Additive Manufacturing Research Centre, Auckland University of Technology Auckland, New Zealand
[b] Department of Biotechnology, PSG College of Technology Coimbatore, India

ARTICLE INFO

*Keywords:*
Microbial
Electrolysis
Cell
Hydrogen
Additive manufacturing
Electrode assembly

ABSTRACT

In the ever-increasing quest for alternative energy sources, hydrogen emerged as a promising green option, but efficient and economical production and management have been the primary constraints. Converting wastewater into $H_2$ and other forms of energy attracted significant attention in terms of simultaneously and sustainably managing both the wastewater and the energy generation problems. Microbial Electrolysis Cells (MEC) evolved recently as promising options for converting wastewater into $H_2$ and electricity but with serious constraints on scalability. The current research aims to explore design and manufacturing solutions to build structurally strong and electrochemically effective electrodes that can also lead to scalable MEC. Two designs based on the interdigitated and spiral electrode architectures are proposed and evaluated. The added design freedom with additive manufacturing by selective laser melting of specific alloys of choice is effectively utilised in physically prototyping the interdigitated and spiral electrode forms designed with controlled porosity constraints. Microstructural, electrochemical, and cell performance characterisations led to the understanding that the spiral electrode configuration with polypyrrole-coated stainless steel 316L anode is a promising design option for both longitudinal and lateral scale-up of the MEC.

## 1. Introduction

The rising demand for energy and the ever-increasing concerns with global warming drive the world towards renewable energy alternatives that can truly be sustainable [1]. Solar [2] and wind energy [3] and bio-electrochemical biomass [4] processing into bioethanol and biodiesel have evolved as possible options but with specific limitations in each case. With the highest energy content at 120 MJ/kg amongst all gaseous fuels, sustainable production from organic wastes, and carbon–neutral end products, hydrogen has recently gained significant popularity as a green fuel [5,6]. Coal gasification [7], oxidation of hydrocarbon [8], biomass gasification [9], electrolysis of water [10], and biological and solar-driven processes are conventional methods used for hydrogen production, but steam reforming and water electrolysis are by far the most widely employed processing routes, though these methods suffer from being highly energy intensive and deriving energy from fossil fuels. Recently, the microbial electrolysis cell (MEC) based on a bio-electrochemical process is drawing attention for hydrogen production utilising biomass as a substrate as it does not require external energy input and reduces the environmental burden [11–14]. Microorganisms grow on the anode surface by harnessing carbon from organic materials while decomposing the biomass substrate into electrons, protons, and $CO_2$ [15]. Exoelectrogens assist the electron transfer from the substrate to the anode [16]. The electrons flow through an external circuit and protons through solutions to the cathode to produce hydrogen as per Equations (1) and (2):

Anode:

$$CH_3COO^- + 4H_2O \rightarrow 2HCO^{3^-} + 9H^+ + 8e^- \quad (1)$$

Cathode:

$$8H^+ + 8e^- \rightarrow 4H_2 \quad (2)$$

The cathode potential of MEC is higher than the anode, so an external voltage (less than 1 V) is required to proceed with the electron transfer. MEC are capable of using wastewater, biomass, organic byproducts, industrial wastewater, animal waste, and food processing waste as fuels.

* Corresponding author.
*E-mail address:* sarat.singamneni@aut.ac.nz (S. Singamneni).

https://doi.org/10.1016/j.matdes.2024.113237
Received 16 February 2024; Received in revised form 9 August 2024; Accepted 9 August 2024
Available online 14 August 2024

However, non-fermentable substrates (acetate) are mainly relied on for energy generation, and their efficiency can reach up to 99 %. Fermentable substrate by-products act as a sink of electrons, so they impact the power output. In addition, fermentable substrates produce organic acids, which reduce the pH value of the solution and inhibit hydrogen production [17].

Based on the configurations, MEC are categorised as single [18] and dual-chamber cells [19]. In a dual-chamber MEC, the cathode and anode are kept in two different chambers, separated by a membrane. Both cation exchange membranes (Nafion) [20] and anion exchange membranes (AMI-7001) [21]are used to help in getting pure hydrogen, avoiding short circuits, reducing the crossover of fuel and bacteria from anode to cathode, and preventing microbial consumption of hydrogen [22]. On the other hand, in a single-chamber MEC, both electrodes are placed in a single chamber, and no membrane is needed. The dual-chamber arrangement renders control of different microbial species in the cathode and anode and reduces bio-contaminations of cathode metal catalysts. The major disadvantage of the dual-chamber arrangement is that the membrane imposes internal resistance, which could be as high as 86 %. Contrarily, the single-chamber cell reduces potential loss caused by the membrane; hence high current densities can be obtained. Other benefits include ease of fabrication and less fouling in the chamber. However, problems such as the consumption of hydrogen by other species of mixed culture (mixing substrates from different sources) and converting hydrogen into methane are likely to arise. Despite these difficulties, single-chamber MEC scores better considering the membrane-less mechanism [23], which makes it easy to build and the higher current densities possible and so the subject of the current research.

Membrane-less single-chamber MECs mainly consist of four parts: anode, cathode, membrane, and fuel source (substrates). The anode is a carbon-based material that imparts average electrical conductivity, biocompatibility, and low overpotential. Carbon paper [24], carbon cloths [25], and graphite felt [26]/granules [27] /brushes [28] have been used for the anode, as these are easily accessible, have better electrical conductivity, biocompatibility, sufficiently low overpotentials, and reasonable prices [29]. These flat electrodes allow the maintenance of a minimum distance between the anode and the cathode, though lack of strength and machinability are drawbacks [30], which are more pronounced when practical and large-scale applications are considered. Due to low specific conductivity, upscaling and the need to provide controlled porosity become difficult aspects to achieve. Anodes with macro-porosity usually perform better than microporous and mesoporous ones, as the bacteria can easily impregnate the macropores. With micro-porous structures, the biofilm can only grow on the surface and is inaccessible to the interior of the anode, leaving the majority of the interior structure unutilised. So, an open and robust three-dimensional (3D) macroporous structure is desired, enabling internal bacterial colonisation and efficient transportation of substrates and thus enhancing the electron transfer process [31]. The anode material is a key factor too in determining the power density and cost of both microbial fuel cells (MFC) and MEC. An MFC is a precursor to the MEC as it is the first step to achieve bacterial acclimation on the anode surface before installing the same into the MEC setup. The ideal MFC/ MEC anode should have a large surface area, low resistance, high corrosion resistance, high biocompatibility, good mechanical strength, and low cost [32].

The cathode supports catalyst materials, which increase hydrogen evolution as well as reduce the activation potential. Platinum is a widely used catalyst, but the high cost and the negative impacts on the environment during platinum extraction restrict its use. On the other hand, SS-304 (mesh) [33], different grades of SS and Ni such as SS 304, SS 316, SS 420, SS A286, Ni 201, Ni 400, Ni 625, Ni HX [34], Carbon cloth [35], Ni foam [36], Ti mesh (Pt 0.5 mg/cm$^2$ catalyst) [37], Stainless steel brush [38] are some of the standard commercially available cathodes used in the literature as another catalyst supporting options due to their low cost, easy availability, and low overpotentials. Olivares-Ramírez et al. employed three different alloys of stainless steel (S.S.) SS 304, SS 316 and SS 430 contain 9.25 %, 12 %, and 0.75 % of nickel, respectively, as a cathode for hydrogen evolution reaction by water electrolysis and it concluded that SS316 is the best material as a cathodic electrode [39]. Call et al. employed a stainless-steel brush as a cathode for hydrogen production. The method witnessed 1.7 $\pm$ 0.1 m$^3$ $H_2$ /m$^3$ d (at current density 188 $\pm$ 10 A/m$^3$) at an applied voltage of 0.6 V. In addition, the stainless steel brush manifested low overpotential needed for activation, and hydrogen throughput was comparable to the costly Pt catalyst-based carbon cloth [40]. Zhang et al. deployed a different-sized mesh made of stainless steel as a cathode in MEC, having a higher surface area than a flat electrode. At an applied voltage of 0.9 V, a hydrogen production rate of 2.1 $\pm$ 0.3 m$^3$ $H_2$ /m$^3$ d (current density of 188 $\pm$ 19 A/m$^3$) was obtained [38]. Evidently, stainless steel, which offers sufficient strength, rigidity, and porosity, is a better alternative to the costly Pt catalyst-based cathode. However, these commercial stainless-steel cathodes have limited manipulability in terms of functional designs and configurations and need a suitable manufacturing method with significantly high design freedom. Controlled porosity is required for better performance in terms of better microbial attachment for an anode. Additionally, porous cathodes render more reaction sites, yielding higher $H_2$ production. Though porous structures made by wire mesh arrangements were attempted, their effectiveness is limited in terms of shape and design. Call and Logan showed fabricating electrodes into shapes that allow them to be close enough, with sufficient rigidity, and maximum interface areas will result in better power densities [30]. Considering the unlimited design freedom in achieving closely controlled macro and mesostructures in complex geometric forms, Additive Manufacturing (AM) is a promising route to explore for making electrodes of suitable topologies. Still, there is no evidence of any previous attempt in this direction. The current paper addresses this, testing the hypotheses that:

- The inherent ability of AM to manufacture highly complex shapes, sizes, and orientations of both electrodes can be exploited to build better electrode systems, targeting intricate electrode geometries with close gaps, leading to higher current densities and more hydrogen recoveries.
- Adding controlled macro porous topologies for the electrodes designed for and manufactured by AM will further enhance the performance of the cells manyfold.

Inherently, microbial electrolysis cell (MEC) based on wastewater treatment require a scalable architecture that provides large surface areas for oxygen reduction at the cathode and bacteria growth on the anode. In earlier research attempts have been made to scale up the system by enlarging the electrode dimensions. Membrane-free tubular cloth electrode assembly (CEA) structures were reported as very compact MEC design options earlier [41]. A two-module tubular electrode MEC was investigated by Gil-Carrera et al. [42], with the sole intention of increasing the surface area to volume ratio. Kim et al. developed a low-cost tubular MFC reactor that could be scalable by longitudinal extension [43]. Zuo et al. introduced a scalable cathode of a tubular ultrafiltration membrane with a conductive graphite coating and a nonprecious metal catalyst (CoTMPP), and the innovative electrode design was attributed to the power density outputs achieved comparable to the use of expensive Pt catalyst-based cathodes [44]. Apparently, tubular electrode designs are promising, but longitudinal scaling is by far the most evaluated design, while lateral scaling attained no attention. Lateral scaling can reduce the aspect ratio, which is not desirable in most cases, but innovative design configurations can alleviate this problem while also effectively achieving reduced space requirements and avoiding dead zones.

Considering the heavy reliance of the performance of MEC on the electrode surface-to-reactor volume ratio, the internal resistance of electrodes, and the mass transfer in the reactor [45], two specific

electrode assembly design options are evaluated in this research: i) Interdigitated and ii) Spiral electrode assembly. Interdigitated electrode assemblies have been employed in various energy-generating fuel cells [46–48] and energy storage supercapacitors [49,50] resulting in much higher throughputs. Following these examples and other reports in the literature, functional interdigitated electrodes made by AM will be the first design consideration to evaluate the proposed hypotheses in this research. In the current study interdigitated and spiral electrodes with controlled porosities are designed fabricated and tested to evaluate the validity of the hypotheses stated above. Additive manufacturing by selective laser melting is employed to fabricate the two forms of electrodes based on AlSi10Mg and stainless steel 316L as candidate materials. Further, surface modification of stainless steel 316L with pyrrole is done using an electrochemical method to enhance acclimation of the electroactive bacteria on the electrodes and eventually the performance output of MEC. XRD, FTIR, and SEM analyses are performed to evaluate the effectiveness of pyrrole coating.

## 2. Materials and methods

### 2.1. Electrode design, fabrication, and surface treatment

SolidWorks package version Rx 2020 is used for all CAD modelling, and the controlled porous structures within the electrode solid geometries are obtained by using the Meshmixer tool (Open-source software offered by Autodesk). Fig. 1 (a) and (b) present the trimetric views of the interdigitated and spiral electrode assembly models respectively along with their critical dimensions. The. stl format file of the CAD model of the basic geometry created in SolidWorks is exported to Meshmixer to generate the uniform lattice utilising the 'make pattern' tool options. The imported geometry is first converted into a solid part with a uniform mesh by using the 'make solid' tab in the tool list. Once the uniform fine mesh is generated, the 'lattice tab' tool is selected as a pattern type with the two inputs i.e. strut thickness and lattice pore size. The final designs of the electrodes, as shown in Fig. 1 (c) and (d), provide a strut thickness of 0.4 mm, and the lattice pore size of 0.8 mm and 0.4 mm for Interdigitated and spiral electrodes, respectively. The gap between the two electrodes is kept at 1 mm. The spiral CAD model is developed with four revolutions going in the counterclockwise direction with a pitch of 5.0 mm, for the physical production of both interdigitated and spiral electrodes with controlled porosity, additive manufacturing technologies are needed. Selective Laser Melting based on the Renishaw AM400 system available at Auckland University of Technology (AUT) is used to print the designed electrode forms. The standard laser melting material options, stainless steel (316L) and Al-Si10-Mg alloy materials commercially made available by Renishaw, are used as the experimental materials for the printing of electrodes. The SLM process conditions for stainless steel 316L include laser power 200 W, scan speed, 570 mm/sec,

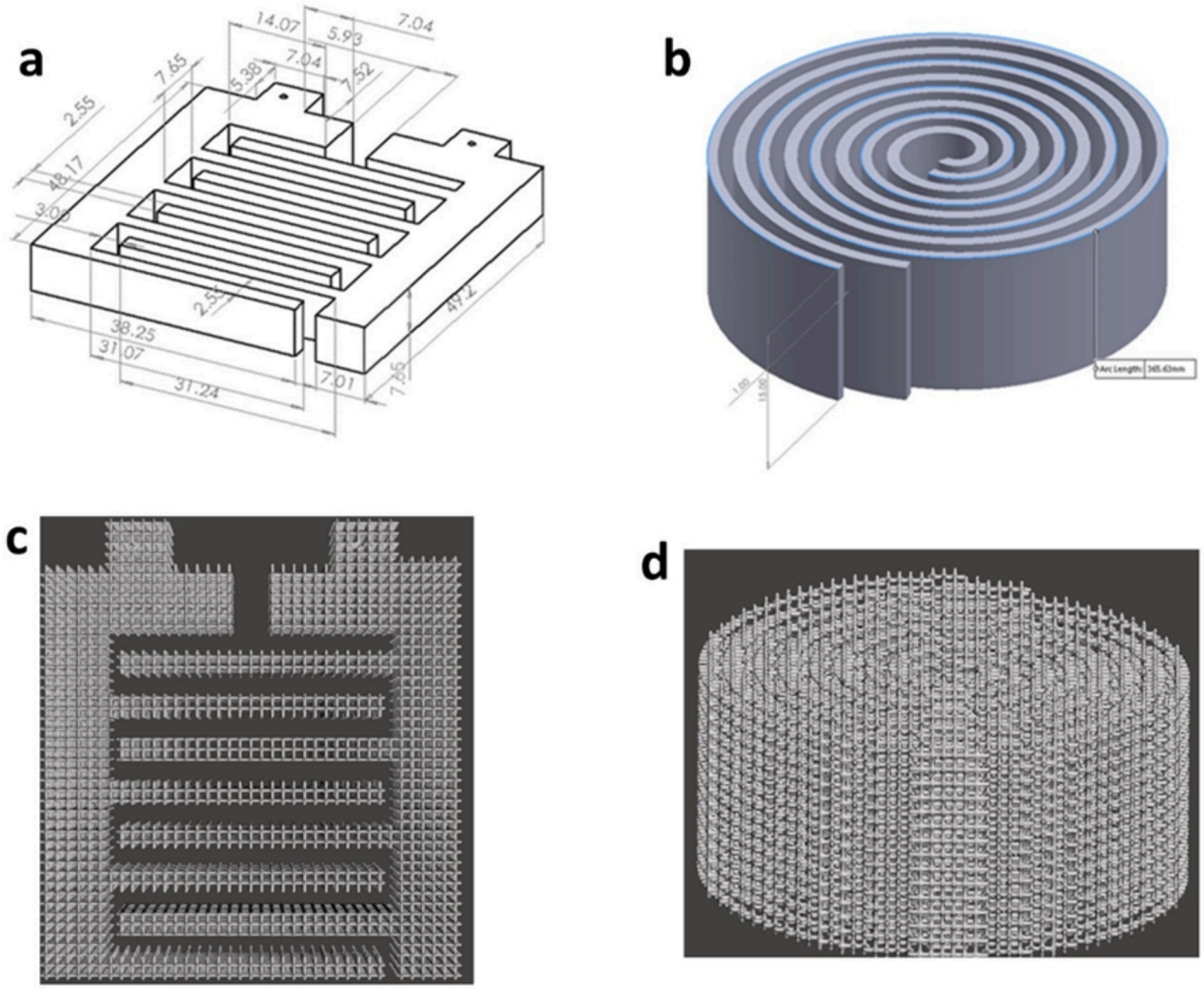


**Fig. 1.** CAD models of (a) Interdigitated electrode assembly, (b) Spiral electrode assembly with the dimension annotated in mm, (c) porous Interdigitated electrode assembly with strut thickness 0.4 mm and strut gap 0.8 mm, and (d) porous spiral electrode assembly with strut thickness 0.4 mm and strut gap 0.4 mm.

layer thickness 40 μm, and hatch spacing 60 μm. Whereas, for AlSi10Mg, the process parameters are laser power 370 W, scan speed 1600 mm/sec, layer thickness 40 μm, and hatch spacing 70 μm. Meander style is used for rasterisation in both cases. For the anode, both stainless steel 316L and Al-Si-Mg are considered, while the cathodes are printed using stainless steel 316L.

Even though stainless steel possesses all the characteristics to be an ideal electrode, it has been rarely used in MFC or MEC applications due to the formation of a passive oxide layer resulting in the strong irreversibility of electron transfer with the bacteria and the consequent reduction in power outputs. Given the low costs compared to carbon cloth, better conductivity, mechanical strength, and the possibility of achieving the required control over porosity using AM, it is pertinent to explore the means of overcoming the issue with the formation of the passivating oxide layers and achieve electron transfer between bacteria and anode. Pu et al. reported that electrochemically depositing polypyrrole onto stainless steel improved corrosion resistance and power density (29 times higher than bare stainless steel anode) [32]. Hou et al. studied surface modifications with three carbon-based coatings: graphene, carbon nanotube, and activated carbon on stainless steel fibre felt. Graphene-modified anode outperformed the three, with a maximum power density of 2142 mW $m^{-2}$ at a current density of 6.1 A/$m^{-2}$(−|-) in MFC [31]. Zheng et al. developed a composite anode made of carbon black and stainless-steel mesh based on a novel binder-free dipping/drying method, and the carbon-black coated anode-based MFC was reported to generate a volumetric current density of 51.0 ± 5.0 mA $cm^{-3}$. Following these examples, the printed stainless-steel electrodes are surface treated using pyrrole coating to act as anodes with increased microbial adhesion and throughput.

The printed stainless-steel anodes are first subjected to ultrasonic cleaning in distilled water for 30 min before applying the electrochemical polymerisation procedure reported earlier [51,52] to apply the polypyrrole coating. The polypyrrole coating procedure is undertaken at the Biotechnology lab, PSG Tech, Coimbatore, India. A two-electrode system based on the cyclic voltammetry method using a Biologic VMP3B-20 Multichannel potentiostat is used to obtain the coating. The working electrode is the printed stainless-steel part, and the counter electrode is a Titanium wire mesh obtained from Aviation Metal and Alloy, India. The pyrrole procured from Sisco Research Laboratories Pvt. Ltd, India, is subjected to vacuum distillation (Hei-VAP Core, Heidolph, Germany) and stored at 4 °C in an inert atmosphere. Vacuum distillation is carried out by filling pyrrole in a flask and placing the same into a rotatory evaporator. Critical process parameters are water bath temperature 60 °C, spinning speed100 rpm, and vacuum pressure 40 mbar. The polymerisation of Pyrrole (0.01 M) on the stainless-steel electrode is carried in 0.5 M p-toluene sulphonic acid (Sisco Research Laboratories Pvt. Ltd, India), which acts as both supporting electrolyte and surfactant. The deposition process is carried out under a potential window ranging between −0.8 to 0.8V for 100 cycles at the scan rate of 10 mV/s. After polymerisation is completed, the electrode is washed using deionised water and dried at room temperature. A cyclic voltammogram representing the polymerisation is presented in supplementary Fig. S1. The Pyrrole-coated electrode after the polymerisation is shown in supplementary Fig. S2.

### 2.2. MEC reactor configuration and processing

A single-chamber wider mouth reactor chamber is used for Hydrogen evaluation. The total volume of the glass reactor is 300 mL (Borosilicate Glass with Polypropylene lid, purchased from Amazon India). All the printed electrodes are cleaned in an ethanol-based sonicator for 3 h and later in deionised water. A titanium wire of 0.3 mm diameter from Aviation Metal and Alloy, India, is used to connect the electrode with external circuits. The printed anode is first enriched in single-chamber MFCs, with carbon cloth as the cathode (0.5 mg/$cm^2$ 60 % Platinum on Vulcan − Carbon Cloth 5*5 $cm^2$, Fuel cell store, U.S.). The MFC is inoculated with domestic wastewater collected from sewage at the hostels in PSG Tech, Coimbatore, India. The MFC is fed a 50:50 mixture of the inoculum and $C_2H_3NaO_2$ (1 g/L) in a 50 mM phosphate buffer, PBS; $Na_2HPO4$, 4.58 g/L; and $NaH_2PO4{\cdot}H_2O$, 2.45 g/L, pH- 7.0, nutrient solution $NH_4Cl$, 0.31 g/L; KCl, 0.13 g/L [28], and vitamin solution and trace mineral solution [53]. A general schematic representation of the single-chamber reactor setup is depicted in Fig. 2.

The MFC setup is kept in an incubator (Rivotek Incubator, India, with Orbital Shaker) maintained at 37 °C. The voltage output reading of the MFC is captured by a datalogger PICOLOG 1216, R.S. components, New Zealand. The biofilm formation based on the MFC is progressed through batch-fed cycles, replacing the medium solution whenever the output is less than 0.1 V across an external resistance of 1000 O. When a reproducible maximum voltage is obtained for three cycles, the anode is considered to be fully acclaimed and transferred to the MEC setup. The MEC reactor setup is fed with the same medium solution as used for feeding the MFC, as discussed above, with sodium acetate (1 g/L) and PBS (50 mM) with trace minerals and vitamins. Methanogenesis inhibition, which eventually maximises the hydrogen production in the MEC reactor, is obtained by adding 100 mM of 2-Bromo ethane sulfonate at 98 % purity obtained from Hychem Laboratories, India, in a medium solution [54].

Before proceeding with the procedure, the reactor is purged with ultra-high-pure (UHP) Nitrogen for 20 min to remove the oxygen. A DC power supply system, ZEAL Model: ZMPS30-10, India, is used to apply constant voltages of 0.6 and 0.9 V. The positive terminal of the power supply is connected to the anode of MEC, and the negative terminal to the cathode through a resistor (Rex = 10 Ω) in series. The voltage (V) output across the external resistor ($R_{ex}$) is recorded every minute (average value) using the PICOLOG 1216 datalogger interfaced with a personal computer. Once the voltage across the external resistor ($R_{ex}$) drops below 5 mV for a given batch of experiments, the solutions in the MEC are replaced. The biogas produced is sampled from the reactor port using Gas sample bags (Tedlar Gas Sampling Bag, Ryan Lab Enterprises, India). The gas sampling bag is vacuumed and sterilised with UHP Nitrogen before use. A Silicon tube (O.D. 5 mm, ID 3 mm, purchased from Local Aquarium Shop, Chennai, India) is used to pass the biogas from the reactor chamber to an airtight gas-collecting Schott bottle (500 mL), filled with water (Saturated NaCl, pH=0.5) [53]. The other port in the Schott bottle is used for the NaCl-saturated water to flow to the measuring cylinder through a silicon tube. The volume of displaced water in the measuring cylinder is equal to the gas collected in the Schott bottle. Total chemical oxygen demand (COD) analysis of the solution is performed at the beginning and end of each batch cycle by following the standard method. The COD analysis of the MEC solution is done following the standard based on the TNT plus COD Reagent, HACH Company, USA. In COD analysis, three samples before the reaction (blank) and after the reaction (each of 2.5 mL) are kept in the glass vial and titrated with a standard solution, and finally, the COD value (mg/L) is calculated following the procedure in reference [36]. The composition of the produced biogas is analysed from the sample gas bag and reactor head space. This analysis of biogas ($H_2$, $CH_4$, $N_2$ and $CO_2$) is done using gas chromatography (Agilent Technologies, 7820-A, Thermal conductivity detector) [55]. Ultra-pure Helium is used as a carrier gas in gas chromatography with a flow rate of 25 mL/min. The cumulative volume (mL) of a specific gas ($V_i$), such as $H_2$, $NO_2$, $CH_4$ and $CO_2$, is calculated using equation (4) [28]:

$$V_i = (H + V_{tot})^* X_i, \tag{4}$$

where $X_i$ is the gas fractions measured by Gas Chromatograph (G.C.) and H headspaces of reactors, and $V_{tot}$ is the total measured volume of all gases at time t. In order to inhibit the growth of methanogens, the lids of the MEC reactor are opened, the medium solution is drained, and the reactor is exposed to air for about half an hour.

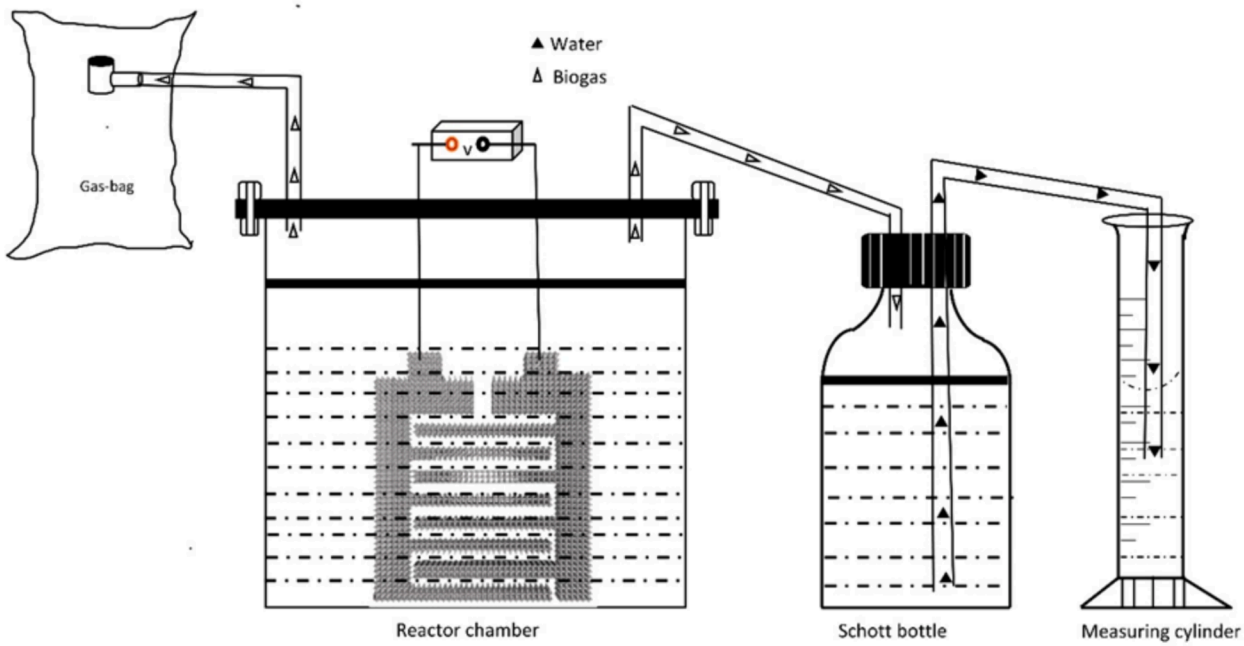


**Fig. 2.** Schematic diagram of the single chamber MEC reactor setup with a water bath, power supply, gas collecting system, and gasbag.

### 2.3. Electrochemical analysis

Electrochemical analysis of microbial activity on the printed anode is done using the Biologic VMP3B-20 Multichannel potentiostat, a two-electrode system by cyclic voltammetry (CV). The comparison is made between the bare printed electrode and the fully acclimated electrode after the exoelectrogen growth on the anode. Cyclic voltammetry is performed on an MFC setup, where the working electrode is an as-printed Al-Si10-Mg interdigitated half electrode, and exoelectrogen acclimated anode, whereas the counter electrode is Pt-coated carbon cloth, and the electrolyte is acetate-based PBS solution. A CV experiment is performed to understand the growth of electroactive bacteria on anodes, and the potential window for CV ranges between – 0.8 to 0.8 V at the scan rate of 10 mV/sec. Before performing CV, the setup is purged with pure Nitrogen to avoid the interaction of oxygen with the electrode [56].

The MEC performance was characterised in terms of Coulombic recovery (C.R.), defined as the total output coulombs over the total input coulombs in acetate. The cathodic hydrogen recovery ($R_{cat}$) is the ratio between the electrons contained in the produced hydrogen gas and the electrons produced as current; the overall hydrogen recovery ($R_{H_2}$) is the substrate used for hydrogen production; the hydrogen production rate ($Q_{H_2}$) is the hydrogen production per anode working volume per time; overall energy recovery ($\eta_{E+S}$) is the ratio of the amount of energy recovered as Hydrogen to the amount of energy added by the substrate and electrical energy [57]. These calculations are done following the references [28,53,57,58].

### 2.4. Hydrogen production rate and yield

Theoretical number of moles $H_2$ ($n_{th}$) produced based on COD removal, is calculated based on equation (5).

$$n_{th} = \frac{\frac{b_{H_2}}{s} V_l \, \Delta COD}{M_s} \tag{5}$$

where $\frac{b_{H_2}}{s}$= 4 mol/mol is the maximum stoichiometric hydrogen production possible from the substrate, $V_l$= 250 mL is the volume of liquid in the reactor, ΔCOD (g COD/L) is the change in substrate concentration over a batch cycle, and $M_S$=82 g/mol is the substrate molecular weight. The COD removal efficiency is calculated using equation (6).

$$\Delta COD = \frac{COD_i - COD_f}{COD_i} \times 100\,\% \tag{6}$$

where $COD_i$ and $COD_f$ are the initial and final COD concentrations of the reactor liquid after each batch of the cycle, respectively. The number of moles of Hydrogen that can be recovered ($n_{CE}$) based on the current produced over one batch is calculated as equation (7).

$$n_{CE} = \frac{\int_{t=0}^{t} I \, dt}{2F} \tag{7}$$

where $I=V/R_{ex}$ is the current (A) calculated from the voltage across the resistor (10 Ω), 2 is used to convert moles of electrons to moles of Hydrogen, F=96 485 Columbs /mole electron is Faraday's constant, and dt (s) is the time interval (1 min) between two data collection. The Coulombic hydrogen recovery ($r_{C_E}$) is given by equation (8), which is the same as columbic efficiency ($C_E$) is the number of moles of Hydrogen recovered in the circuit over the number of moles of Hydrogen theoretically available from the substrate.

$$r_{C_E} = C_E = \frac{n_{CE}}{n_{th}} \tag{8}$$

The cathodic hydrogen recovery $r_{cat}$ is calculated by equation (9).

$$r_{cat} = \frac{n_{H_2}}{n_{CE}} \tag{9}$$

where $n_{H_2}$ is the number of moles of Hydrogen recovered during a batch cycle.

The hydrogen recovery ($r_{H_2}$) is a significant index for MEC performance, which is defined as the ratio of the hydrogen recovered ($n_{H_2}$) and the maximum theoretical hydrogen produced based on substrate utilisation ($n_{th}$), or simply is the substrate used for the hydrogen production, calculated based on equation (10).

$$r_{H_2} = \frac{n_{H_2}}{n_{th}} \tag{10}$$

The Hydrogen yield ($\gamma_{H_2}$) is the ratio of Hydrogen produced ($n_{H_2}$) to the substrate ($n_s$) added.

The maximum volumetric hydrogen production rate (Q) measured by the reactor per day ($m^3$ $H_2$/$m^3$ d) is given by equation (11).

$$Q_{H_2} = 3.68{*}10^{-5}\, I_v\, T\, r_{cat} \tag{11}$$

where $I_v$ (A/$m^3$) is the volumetric current density, obtained as averaged over a 4 h period of maximum current production for each batch cycle. Temperature (T) is in Kelvin and $r_{cat}$ is the cathodic hydrogen recovery.

### 2.5. Energy recovery and efficiency

The amount of energy added to the circuit by the power source that accounted for losses across the resistor (WE) is given in equation (12).

$$W_E = \sum_{1}^{n} (IE_{ap}\,\Delta t - I^2 R_{ex}\,\Delta t) \tag{12}$$

where I (A) is the current calculated as before, $E_{ap}$ (V) is the applied voltage using the DC power source. Δt (1 min) is the time increment for n data points measured during a batch cycle. The amount of energy added by the substrates is given by equation (13).

$$W_s = \Delta H_s n_s \tag{13}$$

where $\Delta H_S$=870.28 kJ/mol is the heat of combustion of the substrate, and $n_S$ is the number of moles of substrate consumed during a batch cycle based on COD removal, calculated by equation (14).

$$n_s = \frac{\Delta COD\, V_{MEC}}{M_s{*}0.78 gCOD{*}g^{-1}} \tag{14}$$

where $M_s$ = 82 g/mol is the sodium acetate molecular weight and 0.78 g COD $g^{-1}$ is the conversion factor of sodium acetate (64/82.4).

The amount of energy recovered as Hydrogen is calculated based on equation (15).

$$W_{H_2} = \Delta H_{H_2}{*} n_{H_2} \tag{15}$$

where $\Delta H_{H_2}$ is the heat of combustion of $H_2$ (285.84 kJ/mol).

The energy efficiency relative to the electrical input ($\eta_E$) is the ratio of the energy content of the Hydrogen produced to the input electrical energy required, calculated by equation (16).

$$\eta_E = \frac{\Delta H_{H_2} n_{H_2}}{W_E} \tag{16}$$

The efficiency relative to the added substrate ($\eta_S$) is given by equation (17).

$$\eta_S = \frac{W_{H_2}}{W_S} \tag{17}$$

The overall energy recovery based on both the electricity and substrate inputs ($\eta_{S+E}$) is given by equation (18).

$$\eta_{S+E} = \frac{W_{H_2}}{W_S + W_E} \tag{18}$$

The percentages of energy contributed by the power source ($e_E$) and substrate ($e_S$) is calculated using equations (19) and (20), respectively.

$$e_E = \frac{W_E}{W_S + W_E} \tag{19}$$

$$e_S = \frac{W_S}{W_S + W_E} \tag{20}$$

## 3. Results and discussion

In the following discussion goes intertwined between two types of electrodes: Interdigitated and spiral. The interdigitated electrode assembly constitutes of the anodic half printed with Al-Si10-Mg alloy subjected to bacterial acclimation in MFC and the cathodic half printed using the SS 316 alloy. With the spiral electrode assembly, the anodic half is printed with two different materials, Al-Si10-Mg alloy (termed as Al) and SS-316 alloy. The anodic half printed with SS-316 is further electrochemically deposited with pyrrole (termed as Ppy-SS). The spiral cathodic half is printed only with SS 316 alloy for both Al-Si10-Mg and Ppy-SS spiral anodic counterparts The anodic halves made by both Al and Ppy-SS are also further acclimated in MFC.

Considering the interdigitated electrode, the anode half printed with Al-Si10-Mg is acclimated first in the MFC along with Pt-coated carbon cloth cathode, inoculum media, and 50 mM PBS solution with acetate. The MFC reactor is inoculated for more than 50 days, replenishing with fresh medium solution as and when the potential falls below 100 mV. The anode is enriched until three cycles are completed, as shown in Fig. 3, after which it is considered fully acclimated. After the three cycles of enrichment in the MFC setup, the biofilm formation or microbial adhesion on the printed anode is confirmed by means of the Field Emission Scanning Electron Microscope (FESEM) analysis. The resulting images, as presented in Fig. 4 for different magnifications, clearly show a thick biofilm formation on the printed anode. The effective bacterial attachment evident in these images is a successful first step towards achieving the charge transfer between bacteria and the anode surface and the overall performance of MEC. Further, cyclic voltammetry is performed to establish the bio-electrochemical behaviour of the printed anode before and after microbial enrichment. Evaluation of electron discharge through cyclic voltammetry helps to understand the growth of electroactive bacteria (EB) on the anode [59]. The cyclic voltammograms presented in Fig. 5 clearly show the peak area of the enriched anode to be larger than that of the as-printed one, indicating higher electrochemical activity of the enriched anode [56].

The acclimated porous anode is then setup in the reactor with the porous stainless steel 316L cathode, completing the interdigitated electrode assembly with a gap of 3 to 5 mm together with the acetate-based PBS solution as substrate as described earlier based on the schematic arrangement shown in Fig. 2. This single chamber membrane-free MEC is applied under constant voltages of 0.6 V and 0.9 V. The experiments are carried out in triplicates, and the data generated is used to calculate the average values and the standard deviations of the critical parameters. The resulting average values and their deviations are listed in Table 1, summarising the performance of the MEC reactors for the applied voltages of 0.6 and 0.9 V. The theoretical concepts and the equations presented in the electrochemical analysis section above are

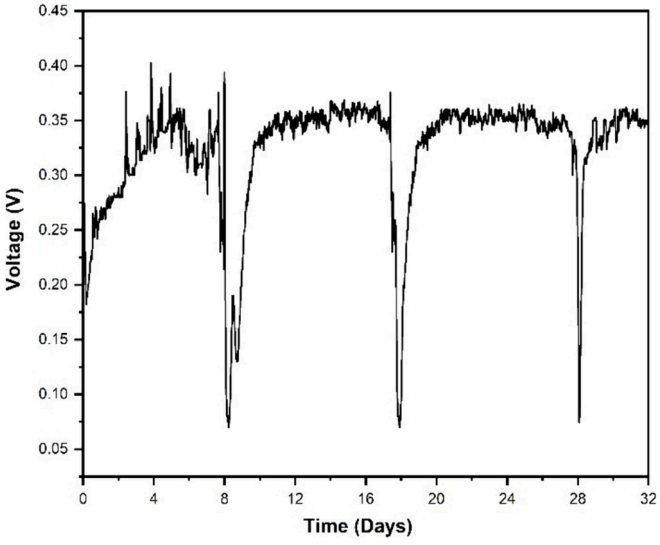


**Fig. 3.** Potential (Volt) *vs* Time (Days) plot of MFC setup for anode acclimation, three cycles completions.

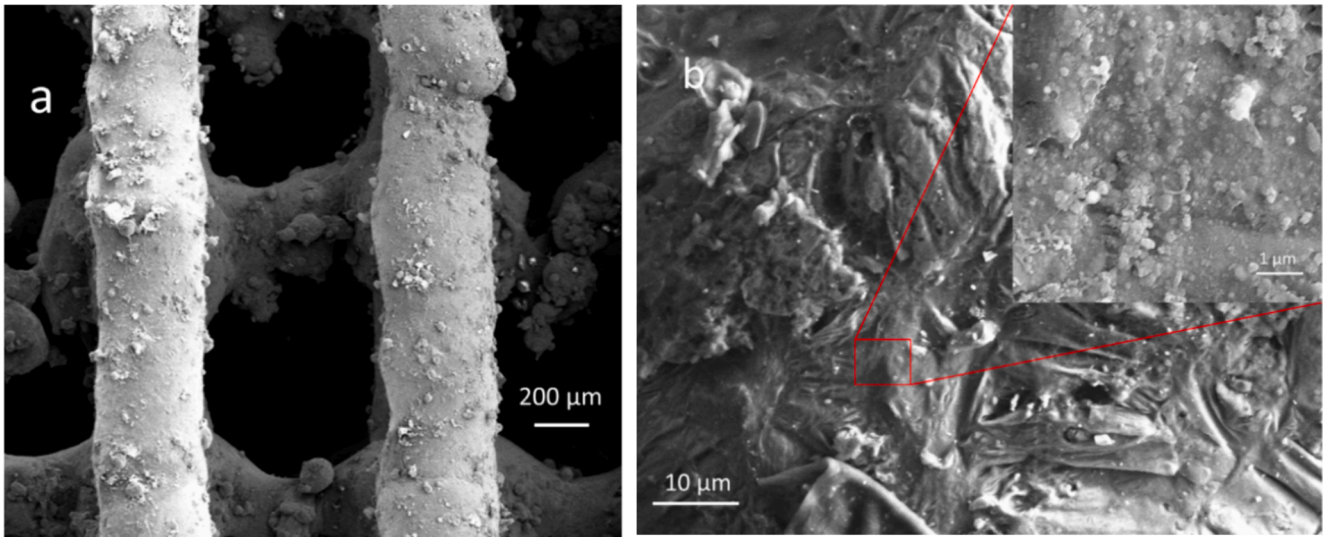


**Fig. 4.** Field Emission Scanning Electron Microscope (FESEM) images of SLM printed Al-Si10-Mg anodic structure after three cycles of enrichment in MFC setup at magnifications, (a) 100 X, (b) 2.5 K X, and inset 20.0 K X.

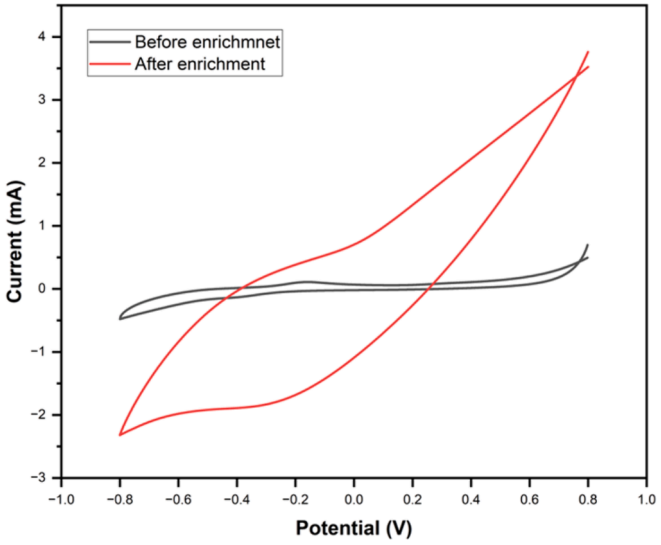


**Fig. 5.** The cyclic voltammograms (CV) plot of Al-Si10-Mg anode, before enrichment (as-printed) and after enrichment (completing three cycles) in MFC, at the applied potential window of −0.8 to 0.8 V and a scan rate of 10 mV/sec.

used in calculating the values listed in Table 1. Considering mainly the volumetric hydrogen production rates in the last column of Table 1, the values obtained are either comparable or even better than many other electrode arrangements reported earlier. However, the carbon fiber-based anode systems studied at 0.9 V external applied voltages showed better results compared to the present one, in particular the combination with the stainless-steel fibre felt reported by Su et al [60] at a $Q_H$ value 3.66 $m^3d^{-1}m^3$ as against the value at around 1.25 $m^3d^{-1}m^3$ attained in the present case. At a first glance, this result does not appear to be spectacularly different from some of the results reported by others, but a more comprehensive comparison including ease and cost of manufacturing is needed to ascertain the true merits of the current materials and methods. This will be undertaken later, after the experimental results from the spiral electrode design are also introduced and discussed.

Now considering the spiral electrode design, first, based on the experiences with the interdigitated model, polypyrrole coating is done on the stainless-steel electrode as an additional measure to enhance the cellular attachment and growth. The characterisation process starts with XRD studies done to evaluate the formation of the thin film on the stainless-steel electrode. The XRD spectrum pattern result as shown in Fig. 6 (a) confirms that the thin film polypyrrole shows an amorphous nature which is similar to the results reported earlier, investigating supercapacitors [61,62]. Fourier transform infrared (FTIR) spectroscopy characterisation is performed in the range of 3500 to 500 $cm^{-1}$ to evaluate the polymerisation of monomers, and the results are shown in Fig. 6(b). The absorption peaks observed at 2920 and 2850 $cm^{-1}$ is the C–H stretching responsible for the weak bands. There is a peak in the C=C bond vibrating at 1559 $cm^{-1}$ [62]. The peak at 1371 $cm^{-1}$ shows C-H plane ring deformation, peaks observed at 1045 and 923 $cm^{-1}$ are due to C=H & N–H plane vibrations, and finally, the peaks obtained at 681 and 537 $cm^{-1}$ are due to polypyrrole ring vibrations [51,52]. The Scanning Electron Microscopy (SEM) image obtained on the coated surface and presented in Fig. 7 ascertains the quality of the electrochemical polymerisation of polypyrrole coating on the printed stainless-steel substrate. The overall impression from the lower magnification image at 150 X is that a compact and homogeneous polypyrrole film is formed on the substrate surface indicating the electro-polymerisation process to be effective [52]. The image in the inset at a higher magnification 20 K X depicts a micro-spherical grain-shaped morphology with microporosity, indicating satisfactory electronic and ionic conductivity [63].

Getting the microbial formation on the electrodes based on the single-chamber membrane-less MFC is done in two setups: first for the as-printed spiral half of the Al-Si10-Mg anode (termed as Al) and second

**Table 1**
Critical responses of the performance of the MECs based on interdigitated electrode assembly operated at applied voltages 0.6 V and 0.9 V.

| Applied voltage (V) | $I_v$(A/$m^3$) | $C_E$(%) | $r_{cat}$(%) | $r_{H_2}$(%) | $\eta_{S+E}$(%) | $\gamma_{H_2}$ | $\frac{e_E}{e_S}$(%) | $Q_{H_2}$($m^3d^{-1}m^3$) |
|---|---|---|---|---|---|---|---|---|
| 0.6 | 84.36 ± 3.47 | 72.8 ± 2.99 | 63.22 ± 2.37 | 46.03 ± 2.13 | 47.64 ± 2.36 | 1.83 ± 0.18 | 26.16 ± 1.58 | 0.59 ± 0.09 |
| 0.9 | 145.72 ± 6.56 | 85.85 ± 4.15 | 75.80 ± 2.06 | 65.08 ± 2.76 | 50.4 ± 2.41 | 2.62 ± 0.34 | 67.89 ± 4.23 | 1.23 ± 0.18 |

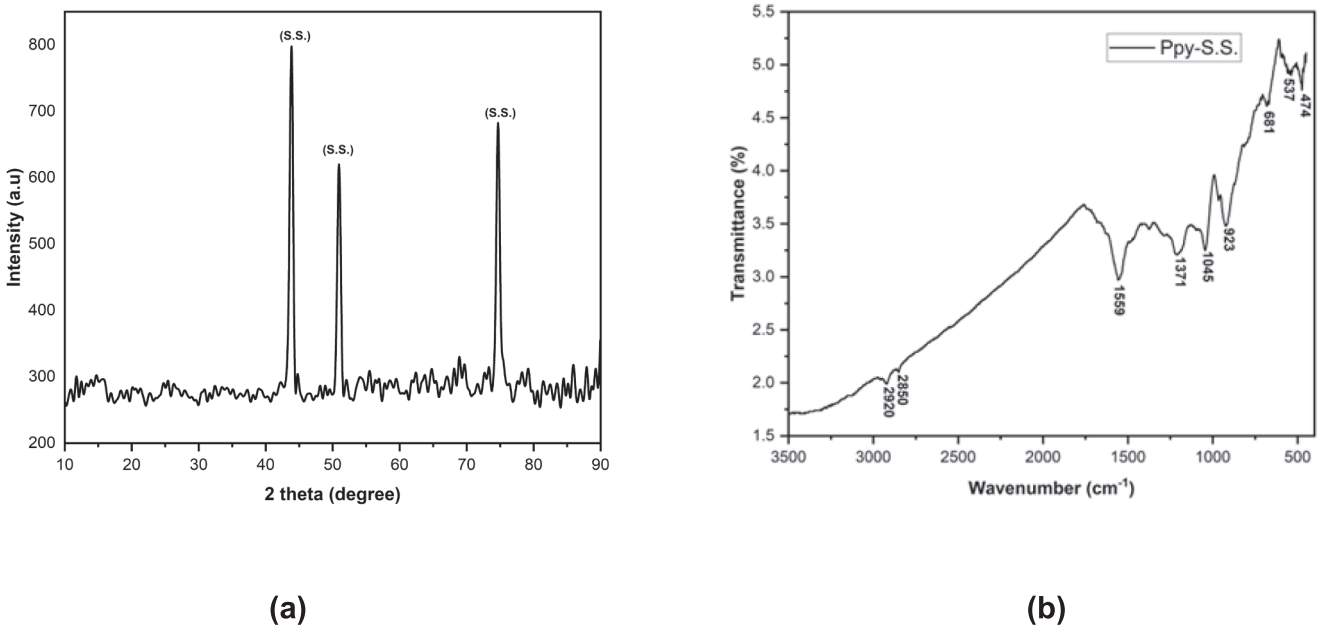


**Fig. 6.** Characterisation of polypyrrole coatings on the stainless steel 316L substrates (a) XRD spectra and (b) Fourier transform infrared (FTIR) spectroscopy results.

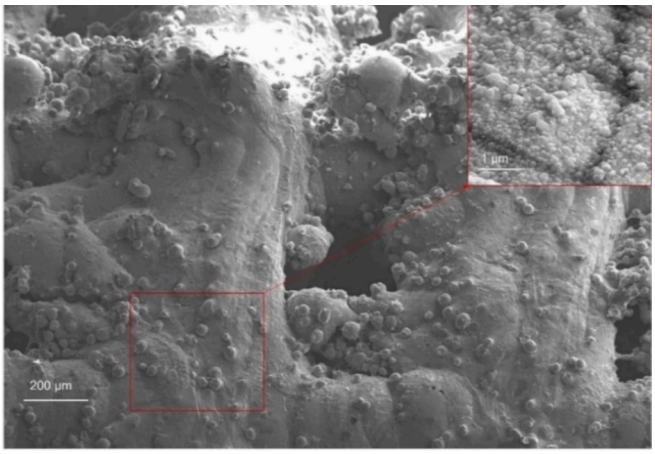


**Fig. 7.** Scanning Electron Microscopy image of polypyrrole coating on the printed stain-less steel 316L electrode at 150 X and 20 kX (inset) magnifications.

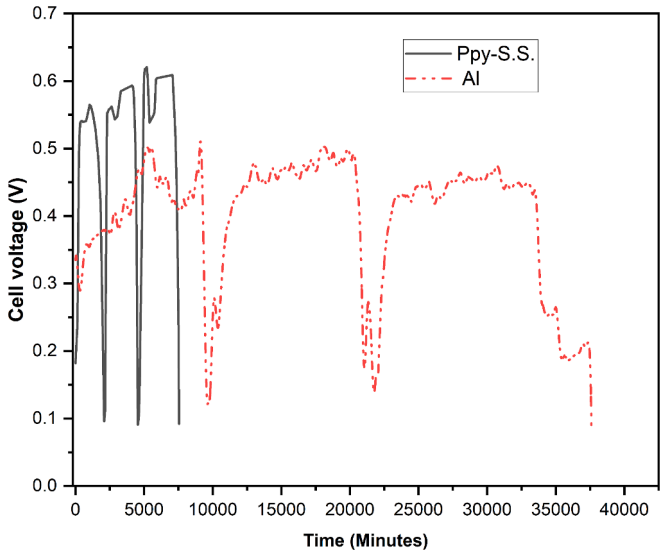


**Fig. 8.** Potential (Volt) *vs* Time (Minutes) plot of MFCs setup for Spiral Aluminium (Al) and Polypyrrole coated stainless steel (Ppy-S.S.) anode acclimation, for three cycles.

for the polypyrrole coated stain-less steel 316 L anode referred as Ppy-SS from here onwards. Other constituents, such as Pt-coated carbon cloth cathode, inoculum media and 50 mM PBS solution with acetate, are the same for both the steps. The MFC reactor is inoculated for more than 50 days for the first setup and 20 days for the second setup and, as is the case with the interdigitated model, replaced with fresh medium solution as and when the potential falls below 100 mV. The anodes are enriched until three-cycles are completed, after which they are considered fully acclimated, as shown in Fig. 8. The voltage *vs* time graph clearly shows that the Ppy-SS anode has more propensity for the growth of electro-active bacteria than the as-printed Al anode. Additionally, the maximum voltage output across 1 kΩ is 0.49 V for the Al-based MFC, whereas the Ppy-SS anode produced 0.61 V. Further, the time for the full acclimation after three cycles is 26 days for the Al anode, while it is only 12 days for the Ppy-SS anode. Compared to the 0.42 V output obtained with the interdigitated Al anode based MFC earlier, the spiral anode MFC voltage output is higher at 0.49 V. This is due to the small pore size lattice of the electrode and the consequent higher pore density in the given volume, leading to the higher accumulation of the exoelectrogen bacteria on the spiral anode.

This is further confirmed observing the enriched biofilm anodes of Spiral half Ai-Si10-Mg anode and polypyrrole coated stainless steel anode, as evident in the Inverted fluorescence microscopy test results shown in Fig. 9. The biofilms formed on the carbon cloth and the printed anodes are stained using bacLight Live/dead bacterial staining kit (Invitrogen, L7012). SYTO9 using propidium iodide stains. The SYTO9 stains the nucleic acid of the live bacteria in green and propidium iodide stains the nucleic acid of the dead bacteria in red. The biofilms are observed under Nikon Ti eclipse fluorescent microscope and images are captured using NIS-elements software. The images are captured under 40X and 100X magnifications. The green fluorescence is directly proportional to the number of live cells in bacterial biofilm. It can be observed that relatively denser biofilm is formed on the Ppy-SS anode

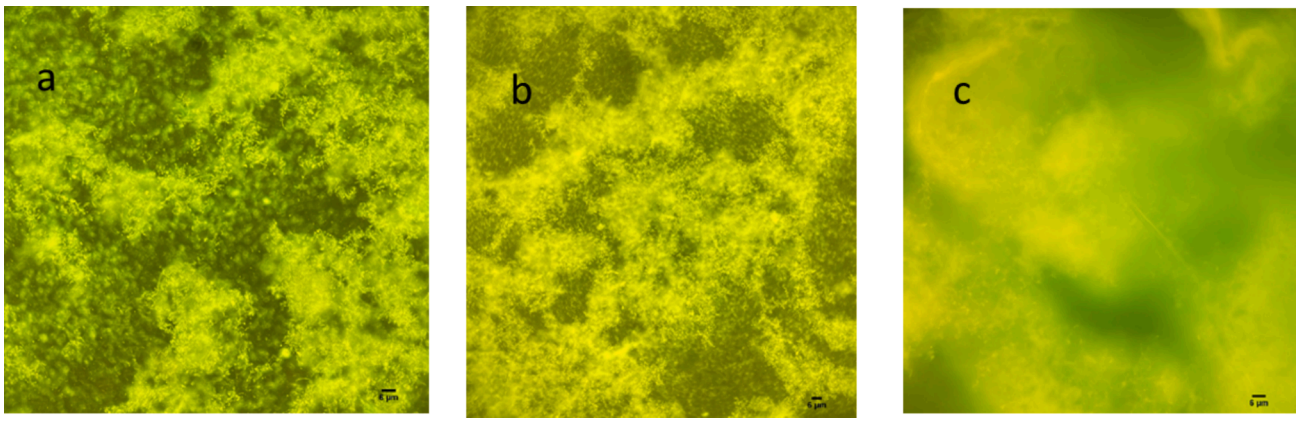


**Fig. 9.** Characterisation of the biofilms on the anodes by fluorescence images, a) indicates the biofilm formed on the porous Spiral half Al-Si10-Mg anode, whilst figures b) and c) indicates the biofilm formed on the Ppy-SS anode. Bar represents 6 μm.

than on the spiral Al anode. Besides, the absence of the red fluorescence indicates that the bacterial biofilm in encompasses live and active bacterial consortia [32].

The acclimated porous Al and Ppy-SS anodes are assembled with stainless steel 316L cathodes as spiral electrode assemblies with the gap in between kept at 1 mm and set up as MECs in the reactor with the acetate-based PBS solution as substrate. Based on the observation that the interdigitated model worked better under the 0.9 V setup, the spiral electrode MECs are applied with 0.9 V. The results of experiments repeated in triplicate and consolidated as average values along with the upper and lower limits are listed in Table 2 to summarise the performance parameters of the MEC for the two different anode setups at 0.9 V applied voltage. A quick glance through the results listed in Table 2 indicates that the Ppy-SS anode-based MEC outperformed the Al based counterpart in every critical response. The superior performance of Ppy-SS anode-based MEC may also be correlated with the higher acclimation or growth of electroactive bacteria on the anode surface, reflected in the inverted fluorescence test result in Fig. 9.

The performance metrics of the interdigitated and spiral electrode configurations tested in the current study are compared with other arrangements reported in the literature, compiling all the critical responses as listed in Table 3. Evidently, carbon-based materials are commonly applied to make the anodes in almost all the other cases reported in the literature, considering the good electrical conductivity and biocompatibility and low overpotentials. The flat surfaces also help maintain close gaps between the anode and the cathode, but strength and other requirements, such as controlled porosity, remain critical bottlenecks towards upscaling. Laser melted aluminium alloy AlSi10Mg was first evaluated by Calignano et al. to print low-density 3D macroporous anodes and observed good affinity for microbial growth based on plate-agar count [64]. Based on these results and also considering the manufacturing freedom with laser melting, the Al alloy anodes are employed for the first time in this work with success as reflected by the results listed in Table 3. Also, Pt catalyst-supported carbon has been the most common option for the cathode, for better hydrogen evolution and reduced activation potentials, but remains highly expensive. Nickel and stainless-steel alloys evolved as alternatives to platinum for their low cost, easy availability, and low overpotentials. Considering the reports listed in Table 3, this is again the first time, laser melted AlSi10Mg and stainless steel 316L cathodes with controlled porosity are evaluated to produce hydrogen in MEC. Table 3 Single chamber membrane-less MEC performance parameters comparison for different anodes and cathode reported in the earlier literatures versus the current study.

### 3.1. *Interdigitated electrodes (Rows 12 and 13 of Table 1)*

With the interdigitated electrode assembly based MEC cases in rows 12 and 13 of Table 3, the current density (A/m$^3$) values increase from 84.36 to 145.72 A/m$^3$ as the applied voltage changes from 0.6 to 0.9 V. Call and Logan [28] reported a similar trend, where current densities increased from 186 to 292 with the applied voltage changing from 0.6 to 0.8 V. The 145.72 A/m$^3$ current density (based on the volume of substrates) at 0.9 V obtained in the current cases is apparently less than most of the other cases compiled in Table 3. However, the volume of substrates is almost nine times more at 250 ml, so the normalised value is lower in this case. For example, Kadier et al. [53] used 750 ml of substrates and obtained a current density of 312 A/m$^3$ only despite using the Ni mesh catalyst cathode, which is comparable to Pt catalyst-based cathode and a higher applied voltage (1.1 V). Columbic efficiency ($C_E$) demonstrate an efficiency of capturing electrons from substrates. A 17.88 % increase in $C_E$ is also evident with the applied voltage increasing from 0.6 V to 0.9 V, which corroborates with Pasupuleti et al. [59] where maximum $C_E$ 1.39 % and 21.18 % were observed at applied currents of 0.1 mA and 1.0 mA respectively. Compared to the other cases, the columbic efficiency values are not that high in the interdigitated design due to the lesser electron capturing capability of Al-Si10-Mg anode compared to the carbon-based alternatives. Despite this, the columbic efficiency values obtained with the interdigitated models at 72.8 % and 85.85 % with 0.6 and 0.9 V respectively are quite reasonable, which is mainly due to the controlled porosity achieved through AM.

The Cathodic hydrogen recovery ($r_{cat}$) obtained is 63.22 % and 75.80 % at 0.6 V and 0.9 V, respectively, comparable to the case reported by Su et al. [60] using stainless-steel mesh and fibre felt with 66.56 % and 78.94 % responses, respectively (Rows 9 and 10 in Table 3), at 0.9 V applied voltage, despite the lesser catalytic activity of stainless

**Table 2**
Critical responses of the performance of the MECs based on the spiral electrode assemblies with electroactive bacteria coated Al and Ppy-SS anodes and stainless steel 316L cathodes operated at 0.9 V.

| Anode material | $I_v$(A/m$^3$) | $C_E$(%) | $r_{cat}$(%) | $r_{H_2}$(%) | $\eta_{S+E}$(%) | $\gamma_{H_2}$ | $\frac{e_E}{e_S}$(%) | $Q_{H_2}$(m$^3$d$^{-1}$m$^3$) |
|---|---|---|---|---|---|---|---|---|
| Al-Si10-Mg | 190.77 ± 10.53 | 93.04 ± 4.65 | 79.14 ± 3.96 | 73.4 ± 3.89 | 66.7 ± 3.33 | 2.94 ± 0.16 | 43.88 ± 2.89 | 1.69 ± 0.13 |
| Ppy −S.S. (316L) | 322.01 ± 17.68 | 100.07 ± 6.54 | 80.18 ± 4.59 | 80.84 ± 4.61 | 88.74 ± 4.95 | 3.23 ± 0.19 | 19.33 ± 0.99 | 2.89 ± 0.18 |

**Table 3**
A comparative evaluation of the MEC configurations evaluated in this study amongst themselves and also with other arrangements reported in the literature.

| No | Applied voltage (V) | Anode | Cathode | $I_v$(A/m$^3$) | $C_E$(%) | $r_{cat}$ (%) | $r_{H_2}$(%) | $\eta_{S+E}$(%) | Substrates | $Q_{H_2}$(m$^3$d$^{-1}$m$^3$) | Reference |
|---|---|---|---|---|---|---|---|---|---|---|---|
| 1 | 0.6 | Carbon cloth | Carbon cloth/ Pt | 9.3 A/m$^2$ * | 75 | 82 | 62 | 58 | Acetate (300 ml) | 0.53 | [25] |
| 2 | 0.6 | Graphite brush | S.S. brush | 188 | – | 84 | – | 78 | Acetate (28 ml) | 1.7 | [40] |
| 3 | 0.6 | Graphite brush | Carbon cloth/ Pt | 186 | 92 | – | – | 80 | Acetate (28 ml) | 1.99 | [28] |
| 4 | 0.6 | Graphite brush | S.S. + $NiO_x$ | 131 | 108 | – | 56 | – | Acetate (28 ml) | 0.76 | [36] |
| 5 | 2.0 | Graphite brush | Carbon cloth/ Pt | 27.8 A/m$^2$ * | 99 | – | – | 34 | Acetate (140 mL) | 1.29 | [13] |
| 6 | 1.1 | Graphite plates | Ni mesh | 312 | 75 | 119 | 89.3 | 62.9 | Acetate (750 mL) | 4.18 | [53] |
| 7 | 0.5 | Graphite-fibre brush | Carbon cloth/ Pt | 106 | 29 | 61 | 17 | – | Swine wastewater (28 ml) | 0.9 | [65] |
| 8 | 0.8 | Carbon Fiber brush | Carbon cloth/ Pt | 158 | 78 | 89 | 68 | 55 | Ethanol-fermentation | 1.52 | [66] |
| 9 | 0.9 | Carbon fiber brush | SS Mesh (316 L) | 290 | 121.83 | 66.56 | 59 | 62 | Acetate (28 ml) | 1.50 | [60] |
| 10 | 0.9 | Carbon fiber brush | SS Fiber felt (316 L) | 484 | 114.70 | 78.94 | 76.37 | 79.61 | Acetate (28 ml) | 3.66 | [60] |
| 11 | 0.9 | Carbon brush | SS Mesh | 4.35 A/m$^2$ * | – | – | – | – | Acetate (28 ml) | 1.25 | [67] |
| 12 | 0.6 | Al alloy | SS 316 L | 84.36 | 72.8 | 63.22 | 46.03 | 47.64 | Acetate (250 ml) | 0.59 | This study interdigitated |
| 13 | 0.9 | Al alloy | SS 316 L | 145.72 | 85.85 | 75.80 | 65.08 | 50.4 | Acetate (250 ml) | 1.23 | This study interdigitated |
| 14 | 0.9 | Al alloy | SS 316 L | 190.77 | 93.04 | 79.14 | 73.4 | 66.7 | Acetate (250 ml) | 1.69 | This study spiral |
| 15 | 0.9 | Ppy-SS | SS 316L | 322.01 | 100.07 | 80.18 | 80.84 | 88.74 | Acetate (250 ml) | 2.89 | This study spiral |

*Current density based on anode surface area.

steel mesh compared to Pt-coated carbon cloth or Ni mesh [54]. The Hydrogen recovery ($r_{H_2}$) values 89.3 % and 89.6 % were reported based on Ni mesh [53] and Ni electroplated Copper base [54] cathodes, while the current study with stainless steel porous cathode resulted a 65.08 % response, which is better than the 59 % obtained with the stainless-steel mesh cathode [60]. The overall efficiency ($\eta_{S+E}$) considers the electrical and substrate energies for hydrogen evolution and the value obtained in the current study is less than those from most of the earlier studies. COD removal efficiency values obtained at 63.25 ± 3.34 % and 71.09 ± 3.98 % for the applied voltages 0.6 V and 0.9 V, respectively, suggest that the substrates have not been fully consumed for hydrogen evolution, indicating the porous stainless steel electrode to be unable to promote catalytic activity comparable to or better than the Pt or Ni-based cathodes [53]. Moreover, the substrate volume is substantially higher in this case than in most of the earlier research, contributing to the lower overall efficiency. The maximum hydrogen generation rate ('Q' per anode working volume per time at 0.6 V is 0.59 m$^3$d$^{-1}$m$^3$, which is higher than the 0.53 m$^3$d$^{-1}$m$^3$ reported for the carbon cloth anode [25]. The porous Al anode provides a higher surface area to volume ratio compared to the carbon cloth anode allowing for better gas production [28], whereas the carbon fiber brush or graphite brush provides even higher Q values due to the higher surface area to volume ratios as evident in most of the other cases (Rows 2 to 11 in Table 3). Further, as the applied voltage increases, the Q value increases [28], because more number electrons are supplied through the external circuit to combine with the $H^+$ ions in the solution to form $H_2$. The hydrogen generation rate at 0.9 V is 1.23, which is more than twice that of 0.6 V. Comparing SS mesh as a cathode in MEC, the current study Q value is comparable to 1.25 [67] and slightly lower than 1.50 [60] at an applied voltage of 0.9 V.

*Spiral electrodes (Rows 14 and 15 of Table 3).*

A quick view of the values in Table 2 clearly elucidates that the Ppy-SS anode-based MEC outperformed the Al alloy-based counterparts in every performance parameter due to the higher acclimation and growth of electroactive bacteria on their surfaces, as evident in the fluorescence test, as shown in Fig. 9. Going back to Table 3, where the results from both the current designs are compared to the other results from the literature, carbon-based materials are the most widely used options for the anode, while the spiral electrode in the current study distinctly differs from this with either Al or Ppy-SS based anodes. With the Al anode and 0.9 V applied voltage, the spiral electrode MEC outperformed the interdigitated counterpart in every performance parameter listed (comparing the results in Rows 13 and 14 in Table 3). Firstly, the inter-electrode gap is 1 mm in the case of the spiral electrode assembly, while the interdigitated electrode assembly has an electrode gap from 2 to 3 mm. The proximity of the electrodes was reported to play a vital role as the closer they are, the better the capability to capture the ions [28]. Secondly, the small pore-size lattice of the spiral electrode results in a higher pore density in the given volume, which eventually leads to higher exoelectrogen bacteria on the spiral anode and more active reaction sites on the spiral cathode.

The current density (A/m$^3$) value obtained for Ppy-SS is 322.01 A/m$^3$, the second highest of all the values compiled in Table 3 (Row 15, Table 3), falling short from only the 484 A/m$^3$ reported by Su et al. (Row 10, Table 3) [60]. It is also pertinent to point out that this value was lower at 290 A/m$^3$ with the stainless steel 316L mesh cathodes used by Su et al., as listed in Row 9 of Table 3. While this electrode is similar to the one used in the current study, the stainless-steel electrode in the current work is produced by selective laser melting with controlled porosity. Also, the polypyrrole coating on the anode seems to have played a positive role in this case. With the stainless steel felt option, Su et al. [60] obtained a better result compared to the current case, possibly due to the better performance of the felt geometry. Further, the pyrrole coating plausibly reduced the pore size of the lattice below 0.4 mm in the current case, as evident in the SEM image of Fig. 7, hindering the medium solution to fully access the internal spaces of the anode. It is pertinent to infer that additional refinement of the pore geometry, optimising it along with the formation of the polypyrrole coating would enhance the performance of the Ppy-SS spiral electrodes further. The coulombic efficiencies ($C_E$) of the spiral Al and Ppy-SS anodes at 93.04 % and 100.07 % respectively clearly indicate better electron capturing from the substrates compared to the 85.85 % obtained with the interdigitated arrangement using the Al anode.

Considering the overall trends in the data presented in Table 3, Pt-coated carbon cloth or Ni alloy-based cathodes score better than the stainless steel cathode counterparts in terms of the cathodic hydrogen recovery ( $r_{cat}$) values mainly due to their better catalytic properties

[54,60]. In similar lines, the $r_{cat}$ values at 79.14 % and 80.18 % for Al and Ppy-SS-based MEC respectively, observed in the current work indicate slight improvements, but still fall short of the performance of the Pt-coated carbon cloth or Ni alloy-based cathodes. With the stainless-steel cathodes at 0.9 V, the spiral model resulted in about a 5 % improvement in $r_{cat}$ values compared to the interdigitated model, possibly due to the smaller mesh size, which renders better reaction sites for the given volume. Similar trends can also be observed for the hydrogen recovery ($n_{H_2}$) responses as well. The Ni and Pt-coated carbon cloth with better catalytic properties have $n_{H_2}$ values 89.3 % and 89.6 % reported for Ni mesh [53] and Ni electroplated copper base cathodes respectively [54], while 73.4 and 80.84 % of hydrogen recovery is observed in the current study with Al and Ppy-SS anodes respectively though far better than the 59 % reported for the stainless steel mesh (Row 9 of Table 3). A major contributing factor is perhaps the 1 mm gap maintained in the spiral electrode assembly, which is far less than the gaps used in other reported cases. Evidently, the smaller gap promotes the more efficient capturing of the charged ions by the cathode as soon as they are generated. Further, the spiral electrode assembly offers the benefits of dual-side reaction sites or dual-facing areas, which further enhance the ion-capturing capabilities.

The overall efficiency ($\eta_{S+E}$) which includes the electrical and substrate energy responses for the hydrogen evolution showed incremental improvements from 50.4 % to 66.7 %, and then to 88.74 % with the Al-interdigitated, Al-spiral and Ppy-SS spiral anode arrangements as reflected in rows 13, 14, and 15 respectively in Table 3. It may be observed that the Ppy-SS spiral electrode-based MEC scored the best at $\eta_{S+E}$ 88.74 %, amongst all the cases reported in Table 3. The reduced gap between electrodes and the finer lattice structures of the electrodes are mainly behind this improvement in the $\eta_{S+E}$ responses. Going back to the results in Table 2, for the Al alloy setup, the energy contributed by the power source ($e_E$) is 30.5 ± 1.57 %, and substrates is 69.5 ± 3.29 %, whereas, for the Ppy-SS setup, power source contribution decreased to 16.20 ± 0.97 % and the contribution by the substrates increased to 83.80 ± 4.34 %. This clearly indicates that the substrates are more effectively utilised in the case of the Ppy-SS MEC setup. The hydrogen yield ($\gamma_{H_2}$) for the Al alloy setup is 2.94 ± 0.16, whereas, for Ppy-SS, it is 3.23 ± 0.19, which represents more moles of hydrogen are produced ($n_{H_2}$) for each mole of

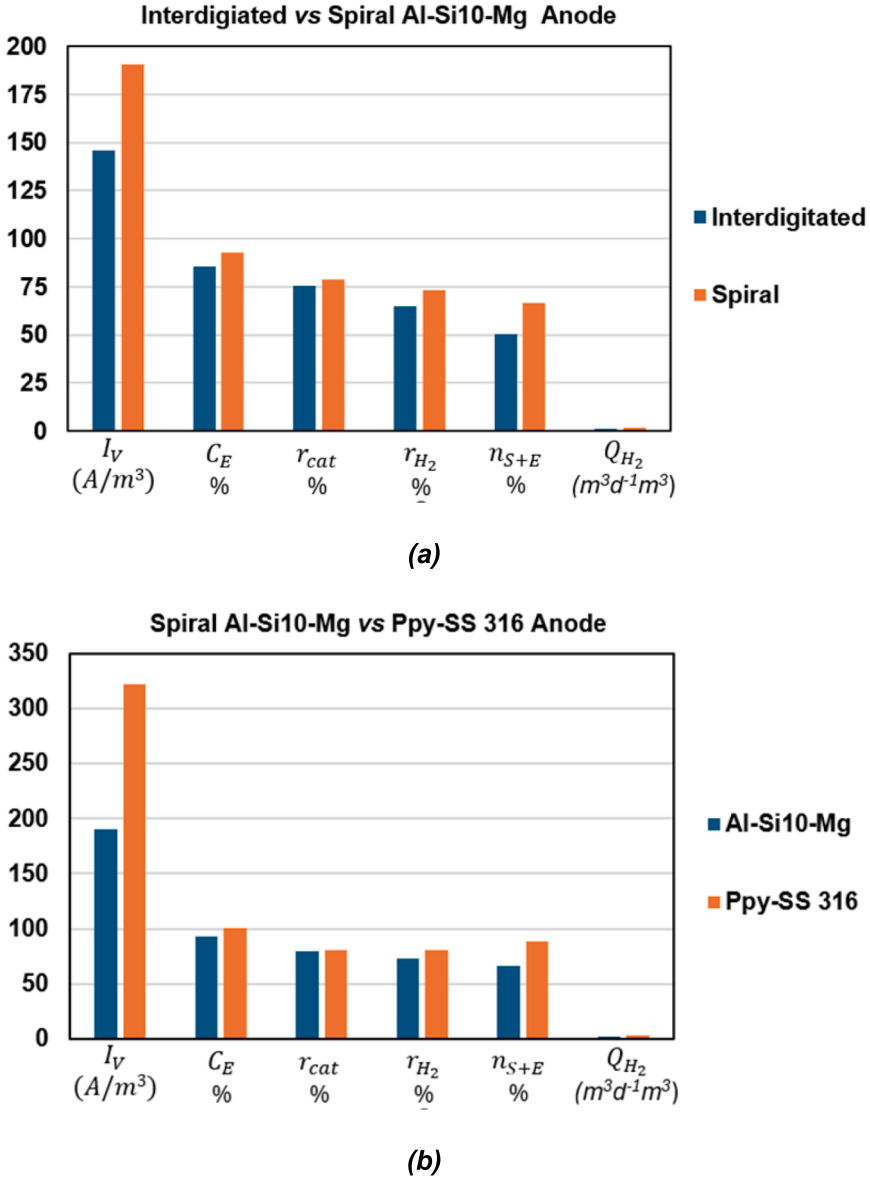


**Fig. 10.** A schematic comparison of the critical responses between (a) interdigitated and spiral electrodes with Al-Si10-Mg anode and (b) spiral Al-Si10-Mg and spiral Ppy-SS 316 anode with the same applied voltage 0.9 V in all the cases.

the substrate ($n_s$) added in the case of Ppy-SS-based MEC. The maximum hydrogen generation rate 'Q' per anode working volume per time is 1.69 ± 0.13 $m^3d^{-1}m^3$ for Al alloy and 2.89 ± 0.18 $m^3d^{-1}m^3$ for the Ppy-SS anode. As already stated (Table 1), the interdigitated Al anode based MEC scored lesser than the 1.50 $m^3d^{-1}m^3$ $H_2$ production reported by Su et al. [60] using stainless steel mesh cathode, but both the Al and the Ppy-SS based spiral MEC surpassed this.

For a better comparison of the critical responses of different combinations of electrodes, relevant data from Table 3 is extracted to draw the bar charts as presented in Fig. 10. Fig. 10 (a) is a graphical comparison of the critical responses of the interdigitated and spiral models with the AlSi10Mg anodes, clearly showing the better performance of the spiral electrode assembly against all critical responses. Fig. 10(b) graphically compares the critical responses of the spiral electrode assemblies based on SlSi10mg and PPy-SS 316 anodes. Though there is a marginal difference in a couple of responses, the Ppy-SS 316 anode outperformed the AlSi10Mg counterpart in all other responses. From this it can be inferred that the close-gap porous spiral electrode assembly is far better in generating $H_2$ than the MEC made of wider-gap flat stainless-steel 316L mesh cathode and carbon fiber brush anode assembly. However, these hydrogen generation levels are lesser when compared to the 3.66 $m^3d^{-1}m^3$ and 4.18 $m^3d^{-1}m^3$ reported to be possible with the stainless-steel 316L fiber felt and Ni mesh electrodes respectively due to the 3D macro-porous structure [60], and the use of highly catalytic electroformed Ni mesh [53] as a cathode material. Based on these observations, it may further be envisioned that optimisation of the 3D microporosity of the cathode, direct printing of porous Ni electrodes, and applying a thin film of catalytic Pt coating of the laser melted stainless steel 316L electrodes can offer further enhancements in the performance of the spiral electrode based MEC.

While the current investigation clearly establishes the proof-of-concept of $H_2$ production from wastewater based on MECs, scalability questions arise both at the electrode and the overall systems levels. There have been many studies in the past evaluating the scaling up of MECs at both system and electrode levels to produce both $H_2$ and electricity at substantial levels, treating both domestic and industrial wastewater [68–71]. One of the major concerns raised was that the $H_2$ production efficiency rapidly decreases with the increase in the size of the reactor, which is predominantly due to the increase in the size of the electrode. However, design alterations as evaluated in the current case will overcome this bottleneck as the porous lattice structures offer increasing reaction areas as the electrode size increases. The current study clearly demonstrated this kind of scale with a relatively smaller size of electrodes. Scaling up of both interdigitated and spiral electrodes is easy to achieve as the new generation laser melting systems are offering much bigger build volumes and multiple lasers operating simultaneously for improved production times. It is also possible that real-world applications in large volume wastewater sources can be implemented by joining a number of laser-melted parts together to construct scaled-up electrodes with controlled porosity and lattice structures.

Another potential issue to be considered is the long-term stability and durability of electrodes especially under continuous operating conditions. Electrode corrosion or deterioration may happen if the cathodic potential imposed is too negative in MEC operation. Catalysts as platinum (Pt), are commonly used in MECs for better dynamics, efficient proton and electron combination and lower overpotentials. However, Pt catalyst is expensive and can be replaced by Palladium (Pd) [72] which is at least 50 times more abundant in nature, cheaper than Pt and offers excellent catalytic performance. Also Molybdenum sulphides ($MoS_X$) are other promising materials for higher HER with excellent chemical stability, and inexpensive which can be used to enhance long term stability [73]. Further, carbon-based materials can also be used in MECs for their biocompatibility, good conductivity, lower overpotentials, and robust stability in a wide range of environmental conditions.

## 4. Conclusions

Additive manufacturing by selective laser melting is employed to fabricate interdigitated and spiral forms of electrodes with controlled porosities with AlSi10Mg and stainless steel 316L materials. The compact and conformal electrode configurations are tested in single-chamber membrane-less microbial electrolysis cells, evaluating the key performance attributes. The hypotheses around the close proximity of the electrodes producing better current densities and the porosities in the electrodes rendering more reacting sites for better hydrogen production are tested and proved to be true through prototype production, experimental evaluation, and the comparative analysis of the results generated. The cyclic voltammetry test results confirmed the bio-electrochemical behaviour of printed anodes before and after microbial enrichment on Al-based interdigitated anodes. XRD, FTIR and SEM results confirmed the effective electrochemical deposition of polypyrrole coating on the stainless-steel anodes. Field Emission Scanning Electron Microscope FESEM results, and the inverted fluorescence images affirmed the microbial growth densities and acclimation of the electroactive bacteria on the electrodes, indicating more promising results with the Ppy-SS anode compared to the Al alloy counterpart. MEC with interdigitated Al anode and stainless steel 316L cathode and spiral Al- and Ppy-SS anodes and stainless steel 316L cathodes are characterised for the overall cell performance responses. The results clearly indicate the Ppy-SS anode-based MEC outperforming the rest of the configurations evaluated in every aspect of characterisation. Further,

- The current density for interdigitated electrode Al-SS based MEC is 84.36 ± 3.47 $A/m^3$ and 145.72 ± 6.56 $A/m^3$, and hydrogen evolution of 0.59 ± 0.09 $m^3d^{-1}m^3$ and1.23 ± 0.18 $m^3d^{-1}m^3$, for applied voltage of 0.6 V and 0.9 V, respectively.
- The current density for spiral Al-SS electrode based MEC is 190.77 ± 10.53 $A/m^3$, and the hydrogen evolution 1.69 ± 0.13 $m^3d^{-1}m^3$ for the applied voltage of 0.9 V.
- The current density for spiral electrode Ppy-SS based MEC is 322.01 ± 17.68 $A/m^3$, which is the second-highest value and hydrogen evolution of 2.89 ± 0.18 $m^3d^{-1}m^3$ the third highest reported values so far in the literature for the single chamber membrane-less MEC.
- The Ppy-SS spiral electrode based MECs scored the best at $\eta_{S+E}$ 88.74 %, amongst all the cases reported so far in the literature, for the Single chamber membrane-less MEC.

Based on the trends from these results it is envisioned that further surface modification of printed stainless-steel 316L using carbon-based material such as graphene, carbon nanotube, activated carbon, and carbon-black can lead to further enhancements in the efficiencies of the MEC. Optimisation of the porosity density and imitating fiber felt geometrical forms can also be promising ways to further improve the cell performance. Platinum coating of the printed optimised porous lattice designs and additive manufacturing of Ni alloy mesh or fiber felt electrodes with optimised porous lattice structures are other avenues for improvements in the future. Leveraging the specific features of nanomaterials of varying morphologies and sizes would provide new opportunities for high-performance electrodes with low cost. In this respect, carbon nanomaterials such as graphene and carbon nanotube (CNTs) can be good options based on their excellent properties such as high aspect ratio, electrical conductivity, and chemical tunability to develop high-performance electrodes. Computational modelling based on generative design tools is another way to optimise the *meso*-structures of electrodes for additive manufacturing and better performance.

## CRediT authorship contribution statement

**Vikash Kumar:** Writing – review & editing, Writing – original draft, Visualization, Validation, Methodology, Investigation, Formal analysis, Conceptualization. **Malaya Prasad Behera:** Writing – review & editing,

Resources, Methodology. **Yifan Lv:** Writing – review & editing, Resources, Methodology. **Banu Pradheepa Kamarajan:** Writing – review & editing, Visualization, Resources, Methodology, Investigation. **Sarat Singamneni:** Writing – review & editing, Supervision, Resources, Project administration, Methodology, Funding acquisition, Conceptualization.

## Declaration of competing interest

The authors declare the following financial interests/personal relationships which may be considered as potential competing interests: Sarat Singamneni reports financial support was provided by Royal Society of Arts NZ. If there are other authors, they declare that they have no known competing financial interests or personal relationships that could have appeared to influence the work reported in this paper.

## Data availability

The authors have not used any data outside of the scope the experimental data already reported in the manuscript. Any data relevant to the experimental results will be provided later, if any user is specifically interested.

## Acknowledgements

The authors wish to acknowledge a part of the support received from the Marsden Grant No. MFP AUT1901 in carrying out the research reported in this paper.

## Appendix A. Supplementary data

Supplementary data to this article can be found online at https://doi.org/10.1016/j.matdes.2024.113237.

## References

[1] U.S. Energy Information Administration, INTERNATIONAL ENERGY OUTLOOK 2021, 2021. https://www.eia.gov/outlooks/ieo/. (Accessed 3 January 2023.
[2] A.O. Maka, J.M. Alabid, Solar energy technology and its roles in sustainable development, Clean Energy 6 (3) (2022) 476–483.
[3] S. Roga, S. Bardhan, Y. Kumar, S.K. Dubey, Recent technology and challenges of wind energy generation: A review, Sustainable Energy Technol. Assess. 52 (2022) 102239.
[4] Á. Ramírez, M. Muñoz-Morales, E. López-Fernández, F. Fernández-Morales, J. Llanos, Advancing circular economy: critical insights into waste biomass derived carbon electrodes for (bio) electrochemical water treatment, Curr. Opin. Electrochem. (2024) 101492.
[5] D. Brus, D. Hotek, Exploring hydrogen fuel cell technology, Technol. Teach. 69 (6) (2010) 20–25.
[6] L. Schlapbach, A. Züttel, Hydrogen-storage materials for mobile applications, Materials for Sustainable Energy, World Scientific Publishing Co.2010, pp. 265-270.
[7] N. Yuan, A. Zhao, Z. Hu, K. Tan, J. Zhang, Preparation and application of porous materials from coal gasification slag for wastewater treatment: A review, Chemosphere 287 (2022) 132227.
[8] I.A. Makaryan, E.A. Salgansky, V.S. Arutyunov, I.V. Sedov, Non-catalytic partial oxidation of hydrocarbon gases to syngas and hydrogen: a systematic review, Energies 16 (6) (2023) 2916.
[9] L.J. Nunes, Biomass gasification as an industrial process with effective proof-of-concept: A comprehensive review on technologies, processes and future developments, Results in Engineering 14 (2022) 100408.
[10] G. Chisholm, T. Zhao, L. Cronin, Hydrogen from water electrolysis, Storing Energy, Elsevier, 2022, pp. 559–591.
[11] R. Gautam, J.K. Nayak, N.V. Ress, R. Steinberger-Wilckens, U.K. Ghosh, Biohydrogen production through microbial electrolysis cell: structural components and influencing factors, Chem. Eng. J. 455 (2023) 140535.
[12] D. Aboelela, M.A. Soliman, Hydrogen production from microbial electrolysis cells powered with microbial fuel cells, Journal of King Saud University-Engineering Sciences (2022).
[13] W. Cui, Y. Lu, C. Zeng, J. Yao, G. Liu, H. Luo, R. Zhang, Hydrogen production in single-chamber microbial electrolysis cell under high applied voltages, Sci. Total Environ. 780 (2021) 146597.
[14] P. Dange, S. Pandit, D. Jadhav, P. Shanmugam, P.K. Gupta, S. Kumar, M. Kumar, Y.-H. Yang, S.K. Bhatia, Recent developments in microbial electrolysis cell-based biohydrogen production utilizing wastewater as a feedstock, Sustainability 13 (16) (2021) 8796.
[15] H. Liu, H. Hu, J. Chignell, Y. Fan, Microbial electrolysis: novel technology for hydrogen production from biomass, Biofuels 1 (1) (2010) 129–142.
[16] S. Cheng, B.E. Logan, Evaluation of catalysts and membranes for high yield biohydrogen production via electrohydrogenesis in microbial electrolysis cells (MECs), Water Sci. Technol. 58 (4) (2008) 853–857.
[17] W. Liu, A. Wang, D. Sun, N. Ren, Y. Zhang, J. Zhou, Characterization of microbial communities during anode biofilm reformation in a two-chambered microbial electrolysis cell (MEC), J. Biotechnol. 157 (4) (2012) 628–632.
[18] F. Ndayisenga, Z. Yu, B. Wang, D. Zhou, Effects of the applied voltage on electroactive microbial biofilm viability and hydrogen production in a recalcitrant organic waste-fed single-chamber membrane-free microbial electrolysis cell performance, Chem. Eng. J. 469 (2023) 144002.
[19] L. Zhang, C. Tian, H. Wang, W. Gu, D. Zheng, M. Cui, X. Wang, X. He, G. Zhan, D. Li, Improving electroautotrophic ammonium production from nitrogen gas by simultaneous carbon dioxide fixation in a dual– chamber microbial electrolysis cell, Bioelectrochemistry 144 (2022) 108044.
[20] R. Cardeña, L. Koók, J. Žitka, P. Bakonyi, B. Galajdová, M. Otmar, N. Nemestóthy, G. Buitrón, Evaluation and ranking of polymeric ion exchange membranes used in microbial electrolysis cells for biohydrogen production, Bioresour. Technol. 319 (2021) 124182.
[21] Y. Choi, D. Kim, H. Choi, J. Cha, G. Baek, C. Lee, A study of electron source preference and its impact on hydrogen production in microbial electrolysis cells fed with synthetic fermentation effluent, Bioengineered 14 (1) (2023) 2244759.
[22] B.E. Logan, B. Hamelers, R. Rozendal, U. Schröder, J. Keller, S. Freguia, P. Aelterman, W. Verstraete, K. Rabaey, Microbial fuel cells: methodology and technology, Environ. Sci. Tech. 40 (17) (2006) 5181–5192.
[23] M. Posadas-Hernández, J.L. García-Rojas, S. Khamkure, L. García-Sánchez, T. Gutierrez-Macías, C. Morales-Morales, E.B. Estrada-Arriaga, Enhanced biohydrogen production in a membraneless single-chamber microbial electrolysis cell during high-strength wastewater treatment: Effect of electrode materials and configurations, Int. J. Hydrogen Energy 48 (2) (2023) 495–513.
[24] J. Ditzig, H. Liu, B.E. Logan, Production of hydrogen from domestic wastewater using a bioelectrochemically assisted microbial reactor (BEAMR), Int. J. Hydrogen Energy 32 (13) (2007) 2296–2304.
[25] H. Hu, Y. Fan, H. Liu, Hydrogen production using single-chamber membrane-free microbial electrolysis cells, Water Res. 42 (15) (2008) 4172–4178.
[26] A.W. Jeremiasse, H.V. Hamelers, M. Saakes, C.J. Buisman, Ni foam cathode enables high volumetric H2 production in a microbial electrolysis cell, Int. J. Hydrogen Energy 35 (23) (2010) 12716–12723.
[27] B. Logan, S. Cheng, V. Watson, G. Estadt, Graphite fiber brush anodes for increased power production in air-cathode microbial fuel cells, Environ. Sci. Tech. 41 (9) (2007) 3341–3346.
[28] D. Call, B.E. Logan, Hydrogen production in a single chamber microbial electrolysis cell lacking a membrane, Environ. Sci. Tech. 42 (9) (2008) 3401–3406.
[29] A. Kadier, Y. Simayi, M.S. Kalil, P. Abdeshahian, A.A. Hamid, A review of the substrates used in microbial electrolysis cells (MECs) for producing sustainable and clean hydrogen gas, Renew. Energy 71 (2014) 466–472.
[30] B.E. Logan, D. Call, S. Cheng, H.V. Hamelers, T.H. Sleutels, A.W. Jeremiasse, R. A. Rozendal, Microbial electrolysis cells for high yield hydrogen gas production from organic matter, Environ. Sci. Tech. 42 (23) (2008) 8630–8640.
[31] J. Hou, Z. Liu, S. Yang, Y. Zhou, Three-dimensional macroporous anodes based on stainless steel fiber felt for high-performance microbial fuel cells, J. Power Sources 258 (2014) 204–209.
[32] K.-B. Pu, Q. Ma, W.-F. Cai, Q.-Y. Chen, Y.-H. Wang, F.-J. Li, Polypyrrole modified stainless steel as high performance anode of microbial fuel cell, Biochem. Eng. J. 132 (2018) 255–261.
[33] R.D. Cusick, B. Bryan, D.S. Parker, M.D. Merrill, M. Mehanna, P.D. Kiely, G. Liu, B. E. Logan, Performance of a pilot-scale continuous flow microbial electrolysis cell fed winery wastewater, Appl. Microbiol. Biotechnol. 89 (2011) 2053–2063.
[34] P.A. Selembo, M.D. Merrill, B.E. Logan, The use of stainless steel and nickel alloys as low-cost cathodes in microbial electrolysis cells, J. Power Sources 190 (2) (2009) 271–278.
[35] L. Xiao, Z. Wen, S. Ci, J. Chen, Z. He, Carbon/iron-based nanorod catalysts for hydrogen production in microbial electrolysis cells, Nano Energy 1 (5) (2012) 751–756.
[36] A.W. Jeremiasse, H.V. Hamelers, C.J. Buisman, Microbial electrolysis cell with a microbial biocathode, Bioelectrochemistry 78 (1) (2010) 39–43.
[37] R.A. Rozendal, H.V. Hamelers, G.J. Euverink, S.J. Metz, C.J. Buisman, Principle and perspectives of hydrogen production through biocatalyzed electrolysis, Int. J. Hydrogen Energy 31 (12) (2006) 1632–1640.
[38] Y. Zhang, M.D. Merrill, B.E. Logan, The use and optimization of stainless steel mesh cathodes in microbial electrolysis cells, Int. J. Hydrogen Energy 35 (21) (2010) 12020–12028.
[39] J. Olivares-Ramírez, M. Campos-Cornelio, J.U. Godínez, E. Borja-Arco, R. Castellanos, Studies on the hydrogen evolution reaction on different stainless steels, Int. J. Hydrogen Energy 32 (15) (2007) 3170–3173.
[40] D.F. Call, M.D. Merrill, B.E. Logan, High surface area stainless steel brushes as cathodes in microbial electrolysis cells, Environ. Sci. Tech. 43 (6) (2009) 2179–2183.
[41] Z. Lai, M. Zhu, X. Yang, J. Wang, S. Li, Optimization of key factors affecting hydrogen production from sugarcane bagasse by a thermophilic anaerobic pure culture, Biotechnol. Biofuels 7 (2014) 1–11.

[42] L. Gil-Carrera, A. Escapa, R. Moreno, A. Morán, Reduced energy consumption during low strength domestic wastewater treatment in a semi-pilot tubular microbial electrolysis cell, J. Environ. Manage. 122 (2013) 1–7.
[43] J.R. Kim, G.C. Premier, F.R. Hawkes, R.M. Dinsdale, A.J. Guwy, Development of a tubular microbial fuel cell (MFC) employing a membrane electrode assembly cathode, J. Power Sources 187 (2) (2009) 393–399.
[44] Y. Zuo, S. Cheng, D. Call, B.E. Logan, Tubular membrane cathodes for scalable power generation in microbial fuel cells, Environ. Sci. Tech. 41 (9) (2007) 3347–3353.
[45] K. Guo, A. Prévoteau, K. Rabaey, A novel tubular microbial electrolysis cell for high rate hydrogen production, J. Power Sources 356 (2017) 484–490.
[46] A. Kazim, H. Liu, P. Forges, Modelling of performance of PEM fuel cells with conventional and interdigitated flow fields, J. Appl. Electrochem. 29 (12) (1999) 1409–1416.
[47] S.-J. Ahn, J.-H. Lee, J. Kim, J. Moon, Single-chamber solid oxide fuel cell with micropatterned interdigitated electrodes, Electrochem. Solid St. 9 (5) (2006) A228.
[48] K. Pandian, M. Ajanth Praveen, S. Hoque, A. Sudeepthi, A. Sen, Continuous electrical lysis of cancer cells in a microfluidic device with passivated interdigitated electrodes, Biomicrofluidics 14 (6) (2020) 064101.
[49] O. Gharbi, D. Jiang, D. Feenstra, S. Kairy, Y. Wu, C. Hutchinson, N. Birbilis, On the corrosion of additively manufactured aluminium alloy AA2024 prepared by selective laser melting, Corros. Sci. 143 (2018) 93–106.
[50] D. Kong, C. Dong, X. Ni, L. Zhang, H. Luo, R. Li, L. Wang, C. Man, X. Li, Superior resistance to hydrogen damage for selective laser melted 316L stainless steel in a proton exchange membrane fuel cell environment, Corros. Sci. 166 (2020) 108425.
[51] S.R. Ananda, M. Murugendrappa, Thermal Studies of Polypyrrole and Cobalt Aluminum Oxide Nano Composites, International Journal of Materials Science 12 (2) (2017) 2017.
[52] J.R. Fried, Polymer science and technology, Pearson Education, 2014.
[53] A. Kadier, Y. Simayi, K. Chandrasekhar, M. Ismail, M.S. Kalil, Hydrogen gas production with an electroformed Ni mesh cathode catalysts in a single-chamber microbial electrolysis cell (MEC), Int. J. Hydrogen Energy 40 (41) (2015) 14095–14103.
[54] A.K. Chaurasia, H. Goyal, P. Mondal, Hydrogen gas production with Ni, Ni–Co and Ni–Co–P electrodeposits as potential cathode catalyst by microbial electrolysis cells, Int. J. Hydrogen Energy 45 (36) (2020) 18250–18265.
[55] N. Montpart, L. Rago, J.A. Baeza, A. Guisasola, Hydrogen production in single chamber microbial electrolysis cells with different complex substrates, Water Res. 68 (2015) 601–615.
[56] P. Wang, H. Li, Z. Du, Polyaniline synthesis by cyclic voltammetry for anodic modification in microbial fuel cells, Int. J. Electrochem. Sci 9 (2014) 2038–2046.
[57] S. Yossan, L. Xiao, P. Prasertsan, Z. He, Hydrogen production in microbial electrolysis cells: choice of catholyte, International Journal of Hydrogen Energy 38 (23) (2013) 9619–9624.
[58] S. Cheng, B.E. Logan, Sustainable and efficient biohydrogen production via electrohydrogenesis, Proceedings of the National Academy of Sciences 104 (47) (2007) 18871–18873.
[59] S.B. Pasupuleti, S. Srikanth, S.V. Mohan, D. Pant, Development of exoelectrogenic bioanode and study on feasibility of hydrogen production using abiotic VITO-CoRE™ and VITO-CASE™ electrodes in a single chamber microbial electrolysis cell (MEC) at low current densities, Bioresour. Technol. 195 (2015) 131–138.
[60] M. Su, L. Wei, Z. Qiu, G. Wang, J. Shen, Hydrogen production in single chamber microbial electrolysis cells with stainless steel fiber felt cathodes, J. Power Sources 301 (2016) 29–34.
[61] P. Kharade, S. Mane, S. Kulkarni, P. Joshi, D. Salunkhe, Ground nut seed like hydrophilic polypyrrole based thin film as a supercapacitor electrode, J. Mater. Sci. Mater. Electron. 27 (2016) 3499–3505.
[62] P.N. Jadhav, K. Sukhatankar, Electrodeposition and characterization of polypyrrole films on stainless steel, Materials Today: Proceedings (2023).
[63] R. Ramya, M. Sangaranarayanan, Analysis of polypyrrole-coated stainless steel electrodes—Estimation of specific capacitances and construction of equivalent circuits, J. Chem. Sci. 120 (2008) 25–31.
[64] F. Calignano, T. Tommasi, D. Manfredi, A. Chiolerio, Additive manufacturing of a microbial fuel cell—a detailed study, Sci. Rep. 5 (1) (2015) 17373.
[65] R.C. Wagner, J.M. Regan, S.-E. Oh, Y. Zuo, B.E. Logan, Hydrogen and methane production from swine wastewater using microbial electrolysis cells, Water Research 43 (5) (2009) 1480–1488.
[66] L. Lu, N. Ren, D. Xing, B.E. Logan, Hydrogen production with effluent from an ethanol–H2-coproducing fermentation reactor using a single-chamber microbial electrolysis cell, Biosens. Bioelectron. 24 (10) (2009) 3055–3060.
[67] F. Li, W. Liu, Y. Sun, W. Ding, S. Cheng, Enhancing hydrogen production with Ni–P coated nickel foam as cathode catalyst in single chamber microbial electrolysis cells, Int. J. Hydrogen Energy 42 (6) (2017) 3641–3646.
[68] V.G. Gude, Wastewater treatment in microbial fuel cells - an overview, J. Clean. Prod. 122 (2016) 287–307.
[69] L. Gil-Carrera, A. Escapa, P. Mehta, G. Santoyo, S. Guiot, A. Morán, B. Tartakovsky, Microbial electrolysis cell scale-up for combined wastewater treatment and hydrogen production, Bioresour. Technol. 130 (2013) 584–591.
[70] R.K. Brown, F. Harnisch, S. Wirth, H. Wahlandt, T. Dockhorn, N. Dichtl, U. Schröder, Evaluating the effects of scaling up on the performance of bioelectrochemical systems using a technical scale microbial electrolysis cell, Bioresour. Technol. 163 (2014) 206–213.
[71] J.A. Baeza, À. Martínez-Miró, J. Guerrero, Y. Ruiz, A. Guisasola, Bioelectrochemical hydrogen production from urban wastewater on a pilot scale, J. Power Sources 356 (2017) 500–509.
[72] W. Wang, B. Zhang, Z. He, Bioelectrochemical deposition of palladium nanoparticles as catalysts by Shewanella oneidensis MR-1 towards enhanced hydrogen production in microbial electrolysis cells, Electrochim. Acta 318 (2019) 794–800.
[73] M. Kokko, F. Bayerköhler, J. Erben, R. Zengerle, P. Kurz, S. Kerzenmacher, Molybdenum sulphides on carbon supports as electrocatalysts for hydrogen evolution in acidic industrial wastewater, Appl. Energy 190 (2017) 1221–1233.